

Photoionized Herbig-Haro objects in the Orion Nebula through deep high-spectral resolution spectroscopy II: HH 204

J. E. MÉNDEZ-DELGADO,^{1,2} C. ESTEBAN,^{1,2} J. GARCÍA-ROJAS,^{1,2} W. J. HENNEY,³ A. MESA-DELGADO,⁴ AND K. Z. ARELLANO-CÓRDOVA⁵

¹ Instituto de Astrofísica de Canarias (IAC), E-38205 La Laguna, Spain

² Departamento de Astrofísica, Universidad de La Laguna, E-38206 La Laguna, Spain

³ Instituto de Radioastronomía y Astrofísica, Universidad Nacional Autónoma de México, Apartado Postal 3-72, 58090 Morelia, Michoacán, Mexico

⁴ Calle Camino Real 64, Icod el Alto, Los Realejos, 38414, Tenerife, Spain

⁵ The University of Texas at Austin, 2515 Speedway Boulevard Stop C1400, Austin, TX 78712, USA

(Received XXX; Revised YYY; Accepted ZZZ)

Submitted to ApJ

ABSTRACT

Contribuciones de Will para el artículo

Keywords: ISM:Abundances – ISM: Herbig–Haro objects – ISM: individual: Orion Nebula – ISM: individual: HH 204

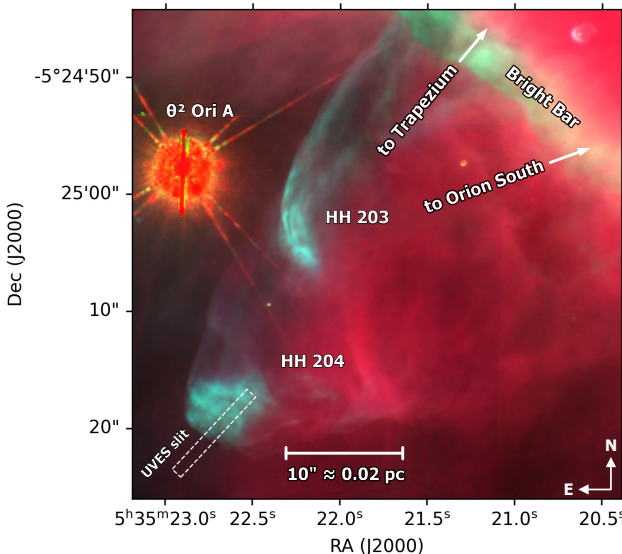


Figure 1. Location of the UVES spectrograph slit at the head of the HH 204 bow shock. The background RGB images shows the immediate environs of HH 203 and 204, derived from *HST* WFPC2 observations (O'Dell & Wong 1996) in filters of [O III] (red), [N II] (green), and H α (blue).

Corresponding author: José E. Méndez-Delgado

1. MATERIAL DE WILL

Pongo primero lo de *HST* porque es más completo.

1.1. Sub-arcsecond imaging of HH 204

Figure 2a shows the ratio of surface brightnesses, $R([O\text{ III}]) = S([O\text{ III}] \lambda 5007)/S(\text{H}\alpha \lambda 6563)$, calculated from *HST* WFPC2 observations in the F502N, F547M, F656N, and F658N filters from program GO5469 (O'Dell & Wong 1996). Flux calibration and correction for contamination by continuum and non-target lines was performed using the coefficients given in O'Dell (2009). It can be seen that the line ratio in the background nebula shows a pronounced gradient from $R([O\text{ III}]) \approx 0.3$ in the north-east to $R([O\text{ III}]) \approx 0.5$ in the south-west.¹ Inside the bow shock, the ratio is significantly smaller, for instance falling from $\simeq 0.4$ to $\simeq 0.2$ along the length of the UVES slit.

However, the most interesting feature of the $R([O\text{ III}])$ image is the slight *increase* in the ratio that is seen in a

jemd@iac.es

¹ For comparison with results from our UVES spectra, and using the average reddening for the HH 204 region (Weilbacher et al. 2015), the conversion is $\lambda 4959/\text{H}\beta \approx 1.1 R([O\text{ III}])$.

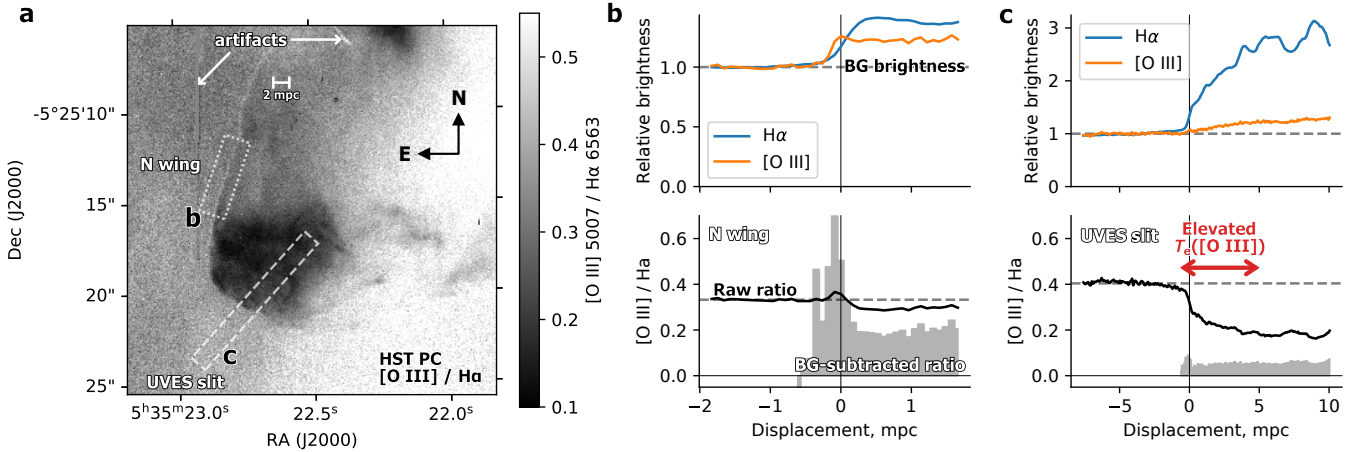


Figure 2. (a) Map of the line ratio $[O\text{ III}]\lambda 5007/\text{H}\alpha\lambda 6563$, calculated from *HST* images with the PC chip of the WFPC2 camera. The position of the UVES spectrograph slit is outlined by a dashed box, while a further region of interest in the N wing of the bow shock is indicated by a dotted box. The vertically oriented ‘scar’ at upper left is an artifact due to the bright star θ^2 Ori A, located just north of the field of view. (b) Average cut profiles of the *HST* images for the box in the N wing that is outlined in panel a. Upper graph shows surface brightness profiles in the two emission lines, normalized to the mean nebular background value outside of the shock. Lower graph shows the line ratio, with the raw ratio indicated by the black solid line and the background-subtracted ratio indicated by the gray histogram. The zero point of the displacement axis is taken to be the location of the maximum gradient in the $\text{H}\alpha$ surface brightness. (c) Same as panel b, but showing average profiles of the *HST* images along the UVES slit. The region of the slit that shows $T_e([O\text{ III}]) > 12\,000\text{ K}$ in the blueshifted component is indicated by the red arrow.

thin layer along the leading edge of the bow shock. This is most clearly visible in the northern wing of HH 204, such as the area highlighted by a dotted outline box in the figure. Average profiles across the shock for this region are shown in Figure 2b. The lower panel shows that the raw ratio (solid black line) increases only slightly above its value in the background nebula, which is because the brightness increase across the bow shock is only a small fraction of the background brightness, as can be appreciated in the upper panel. In order to isolate the emission of the shocked gas from that of the nebula, we calculate the background-subtracted line ratio:

$$R'([O\text{ III}]) = \frac{S([O\text{ III}]) - S_{BG}([O\text{ III}])}{S(\text{H}\alpha) - S_{BG}(\text{H}\alpha)} \quad (1)$$

under the assumption that S_{BG} for each line is constant along the profile. The result is shown as a gray histogram in the lower panel of the figure, which reveals a sharp peak of width $\approx 0.3\text{ mpc}$ that reaches a maximum value $R'([O\text{ III}]) \approx 2R_{BG}([O\text{ III}])$ and is centered on a displacement of $\approx -0.1\text{ mpc}$. The origin of the displacement axis is set to the peak in the spatial gradient of the $\text{H}\alpha$ surface brightness, corresponding to the outer edge of the dense shocked shell. The negative displacement of the $R'([O\text{ III}])$ peak means that this occurs *outside* the dense shell, closer to the shock front itself.

Figure 2c shows the same quantities calculated along a cut that coincides with our UVES slit at the head of HH 204. In this case, $R'([O\text{ III}])$ is always signifi-

cantly less than $R_{BG}([O\text{ III}])$, but it does still show a small local peak with a position and width that is similar to the more impressive one in the northern wing. These peaks in $R'([O\text{ III}])$ occur over a much smaller scale than any of spatial gradients that we find in our UVES slit spectra and are only detectable because of the high spatial resolution of the *HST*.² For example, the increase in $T_e([O\text{ III}])$ that we detect in the blue-shifted emission near the shock front (Figure 6) occurs over a scale of 5 mpc , indicated by the red arrow in the figure, which is more than 10 times larger than the width of the $R'([O\text{ III}])$ peak.

Lo que sigue es más bien discusión

What is the origin of the narrow peak in the $[O\text{ III}]/\text{H}\alpha$ ratio that is seen just outside the shocked shell? When a shock propagates into low-ionization gas (predominantly O^+), there are three zones where enhanced $[O\text{ III}]$ emission might be expected (Cox & Raymond 1985; Sutherland & Dopita 2017): first, the radiative precursor in the pre-shock gas; second, the non-equilibrium collisional ionization zone immediately after the shock; third, the radiative relaxation zone where the post-shock gas cools back down to the photoionization equilibrium temperature of $\sim 10^4\text{ K}$. The first of these can be ruled out in the case of HH 204 because the pre-shock photoioniza-

² Pixel size of 0.045 arcsec , which well samples the PSF width at $\text{H}\alpha$ of 0.083 arcsec .

tion of O^+ would require shock velocities greater than 150 km s^{-1} , observed proper motion and radial velocities imply a shock velocity less than 100 km s^{-1} . The second zone has a high temperature ($> 50\,000 \text{ K}$ for shock velocities $> 55 \text{ km s}^{-1}$) but is severely under-ionized, resulting in line emissivities that are far in excess of the equilibrium values in a very thin layer. The third zone, in which oxygen is recombining through the O^{++} stage while cooling through the range $30\,000 \text{ K}$ to $10\,000 \text{ K}$ is predicted to be somewhat thicker and with a higher electron density, yielding a greater contribution to the total $[O \text{ III}]$ emission. Given the electron density that we derive of $13\,500 \text{ cm}^{-3}$ (Table 3), and assuming a shock velocity $< 70 \text{ km s}^{-1}$, the cooling length should be approximately 0.05 mpc , or 0.025 arcsec , which is a few times smaller than the *HST* resolution. However, this analysis applies only to the head of the bow shock. In the wings, the shock is not perpendicular to the upstream gas velocity, but is oblique at an angle α . This yields a post-shock equilibrium density that is smaller by a factor of $\cos^2 \alpha$, and a cooling length that is larger by the same factor. Hence, the cooling length is expected to be resolved for α smaller than about 45° , which is consistent with our observations of the narrow peak in the $[O \text{ III}]/H\alpha$ ratio in the north wing. The reason that the same behaviour is not seen in the opposite wing is probably that the ambient nebular emission is much more highly ionized there, which masks the effect.

Note that the length scales over which we see changes in $T([O \text{ III}])$ from the UVES data are much larger than this ($\approx 5 \text{ mpc}$, see Figure 7), and so cannot be ascribed to the cooling zone behavior described above. Instead, we suggest that we are seeing the superposition of two different emission components: one from the bow shock and one from the Mach disk (the shock internal to the jet). The jet shock will have a lower Mach number, \mathcal{M} , than the bow shock so long as the unshocked jet is denser than the ambient medium, as appears to be the case in HH 204. The thickness of the equilibrium (cooled) shocked shell is proportional to \mathcal{M}^{-1} and so should be larger for the shell behind the Mach disk, which thus dominates the emission in much of the slit (displacements 5 to 12 mpc in Figure 7). At smaller displacements, the contribution of the bow shock gets progressively larger, thus explaining the increase in $T([O \text{ III}])$. The expected length scale for this variation is roughly the radius of curvature of the bow shock, which agrees with the observed 5 mpc . The only reason that this effect is visible at all is that $[O \text{ III}]$ emission from the equilibrium shell is so weak. For lower ionization lines, the contribution of the bow shock to the total brightness is always negligible, even for positions close to the shock.

1.2. Origin of the jet that drives HH 204

At least two different high-velocity flows converge on the general HH 203/204 region from the direction of the inner Orion Nebula (see Figure 3), but it is not clear if either of them are directly responsible for driving the HH 204 bow shock. One flow is at a position angle (PA) of $\approx 118^\circ$ and transitions from a high ionization state north-west of the Bright Bar (cyan contours in Fig. 3a), to a lower ionization state (yellow contours) to the south-east of the Bright Bar. The other is at PA $\approx 140^\circ$ and is of low ionization for its entire detected length. Both these flows give the appearance of driving HH 203, which implies that HH 203 may be a superposition of two unrelated bow shocks. Such a superposition is consistent with the detection of two different velocity components (-73 and -39 km s^{-1}) at the head of the bow shock, and also with the complex structure apparent in high-resolution *HST* images (see Fig. 3b). O'Dell et al. (2015) noted that in addition to the main bow shock (HH 203a), there appears to be a second faint bow shock (HH 203b), associated with the PA118 flow. We also detect a third faint bow shock, which we denote HH 203c, situated in front (SW) of HH 204a. Note that O'Dell et al. (2015) give position angles of 124° and 127° , respectively, for HH 203 and HH 204, which probably represent an average of the PA118 and PA140 flows.

The southern portion of HH 203a, which we label as “[S II] knot” in the figure, is particularly strong in the [S II] and [O I] filters and coincides with the peak of the -39 km s^{-1} feature. The spatial alignment and the similarity in velocity and ionization makes it likely that this knot is part of the PA140 flow. It is conceivable that this flow may extend farther to the SW and be driving the HH 204 bow shock, although there is no direct evidence for this. On the other hand, a third flow at PA $\approx 108^\circ$ is seen to feed into HH 204 from the west. This jet, first noted by Doi et al. (2004), is very short and stubby, and can be traced back only 10 arcsec (20 mpc) from the bow shock. There is another faint filament of high-velocity [O III] emission that extends between the HH 203 and HH 204 regions at PA $\approx 108^\circ$ (see Fig. 3a). This appears to provide a connecting bridge between the PA140 and PA108 flows, although the difference in velocity and ionization with respect to the PA108 flow argues against a physical association with HH 204.

We have searched archival observations in other wavebands for any evidence of jets along the back projection of the PA108 axis. The most convincing association is with a molecular hydrogen filament seen in the $2.12 \mu\text{m}$ line (see Figure 3e). At the position of this filament, HH 204 is at PA = 105° , which is well within the uncer-

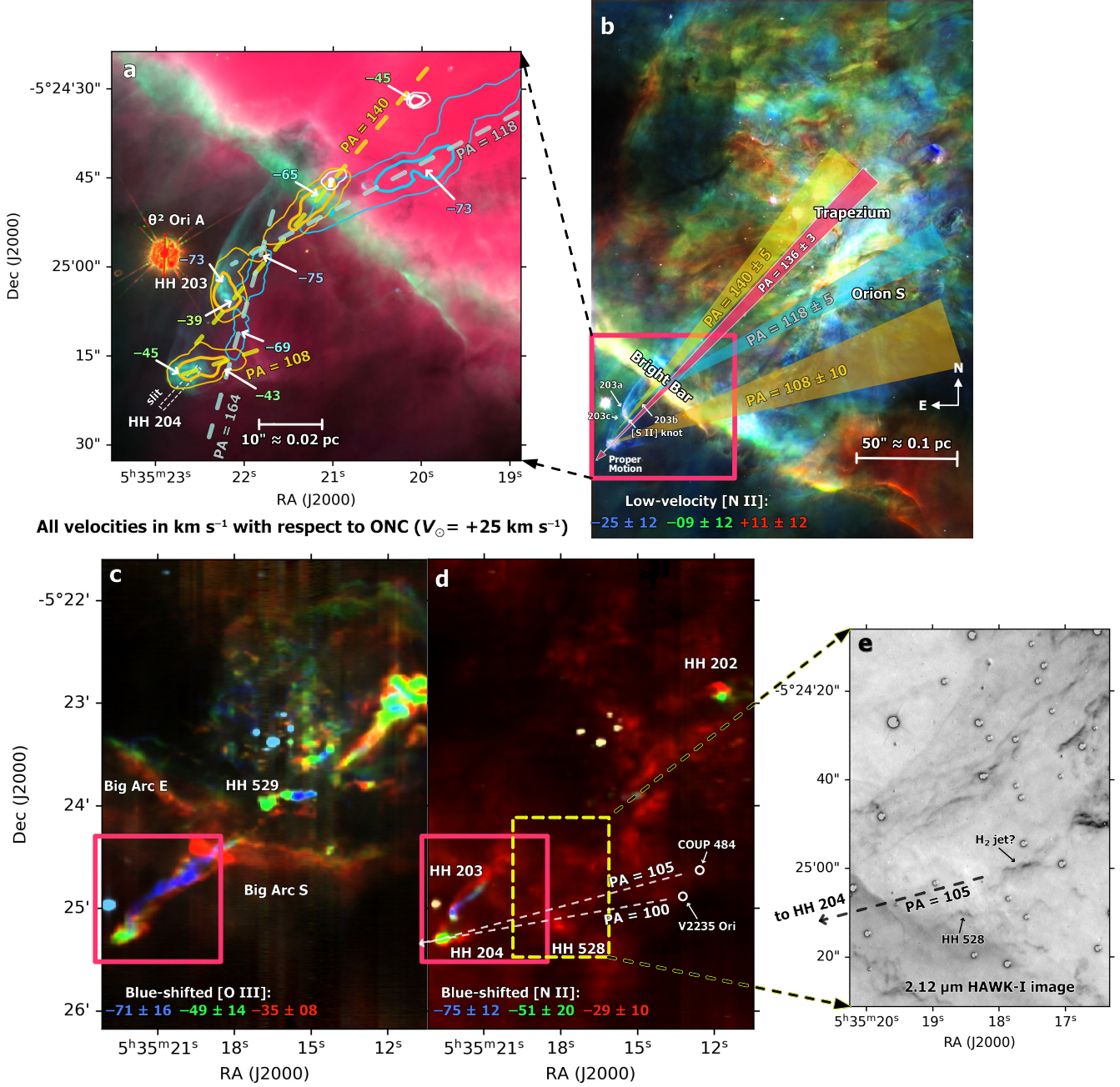


Figure 3. Location of HH 204 within the Orion Nebula. (a) Same as Figure 1 but showing an expanded view of the bow shocks and possible driving jets. Contours show highly blue-shifted emission of [O III] (cyan, centered on -70 km s^{-1}) and [N II] (yellow, centered on -50 km s^{-1} , and white, centered on -35 km s^{-1}), derived from multiple longslit spectra (Doi et al. 2004 as recalibrated in spectral atlas of García-Díaz et al. 2008). Mean velocities with respect to the Orion Nebular Cluster of particular features related to the HH objects are indicate by arrows. (b) Location of HH 204 with respect to the inner Orion Nebula. The intensity of the image comes from the [N II] *HST* WFPC2 observations, but colorized according to the velocity of the slow-moving nebular gas (within about 30 km s^{-1} of the systemic velocity) as derived from the longslit spectra, see color key on figure. (c) Highly blue-shifted [O III] emission for a field of view similar to that of panel b. (d) As panel c but for highly blue-shifted [N II] emission. Two candidate stellar sources along the back-projection of the PA108 flow are indicated by white circles (see discussion in text). (e) Near-infrared HAWK-I imaging of the region outlined by a yellow dashed box in panel d in the $2.12 \mu\text{m}$ H_2 line (Kissler-Patig et al. 2008), showing an emission filament that may be associated with HH 204.

tainties, and the orientation of the filament is consistent with the same PA. Unfortunately, no kinematic observations are currently available for this filament, so its association with HH 204 can only be tentative. The stellar source that best aligns with the H₂ filament is COUP 484, see Figure 3e. However, this is a rather low luminosity star and therefore seems an unlikely candidate for driving such an impressive large-scale outflow. The star V2235 Ori is also marginally consistent within the uncertainty with the PA108 axis and is roughly 100 times brighter than COUP 484 in the K and L infrared bands (Muench et al. 2002), but its position is completely inconsistent with being the source of the H₂ filament. There is also marginal evidence from MUSE observations (Weilbacher et al. 2015) for a blue-shifted [Fe III] filament that extends from the position of the H₂ filament towards HH 204, but the data are noisy.

A further important line of evidence for the flow direction is provided by proper motion measurements. We have re-measured the proper motions using *HST* images over an interval of 19 years (1996 to 2015) using the methodology described in section 10 of Paper I. For the “nose” of the HH 204 bow shock, we find a plane-of-sky velocity of (71 ± 9) km s⁻¹ at PA = $(136 \pm 3)^\circ$. After correcting to a common distance of 417 pc the previous measurements of Doi et al. (2002) are (83 ± 10) km s⁻¹ at PA = $(137 \pm 7)^\circ$, which are consistent with our measurements within the uncertainties. The proper motion axis is shown by a large red arrow in Figure 3b for comparison with the candidate axes from the high radial velocity jets. It is marginally consistent with the PA140 axis, but not all with the PA108, PA118, or PA164 axes.

In summary, convincing evidence for which large scale flow might be driving the HH 204 bow shock is frustratingly absent. Although the PA108 flow is clearly associated with HH 204, its short length means that the exact orientation is very uncertain. The PA140 flow has a much better defined direction, but its extension beyond the position of the [S II] knot in order to feed into the HH 204 bow shock is purely speculative. However, the close agreement between this flow direction and the proper motion axis is an additional argument in its favor. The only thing that can be said with any degree of certainty is that the high-ionization PA118 flow is *not* driving HH 204, but only HH 203.

In Figure 3b we show the back projection of all three of these flows into the core of the nebula, assuming an uncertainty of $\pm 10^\circ$ for the PA108 flow and $\pm 5^\circ$ for the other two. The PA118 flow is consistent with an origin in the Orion S star forming region, as has been remarked many times previously (O’Dell et al. 1997; Rosado et al. 2002; O’Dell & Doi 2003). However, neither of the other

flows are consistent with an origin in that region, unless the flow has suffered a relatively large-angle deviation. The back-projection of the PA108 flow falls significantly to the south of the main Orion S region in an area with no convincing candidates for the driving source (see above discussion of the possible H₂ jet). The back-projection of the PA140 flow intersects the Trapezium stars in the very center of the nebula, which raises the possibility that the source may be a proplyd, which are highly concentrated in that region.

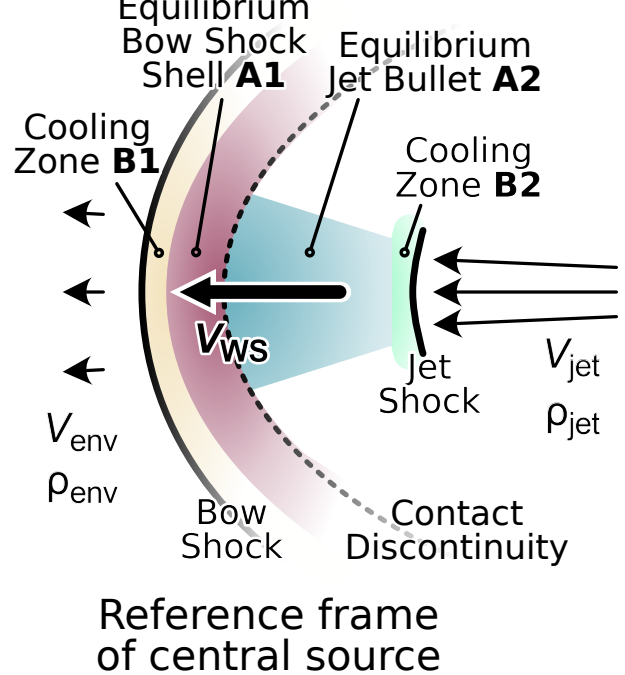
2. TWO-ZONE MODEL FOR OBSERVED TEMPERATURE STRUCTURE

At each position along the spectrograph slit, the line of sight will cross several zones with different physical conditions. These may include:

- A1:** The compressed shell behind the bow-shock, which is in photoionization equilibrium;
- A2:** The main body of the jet bullet, also in photoionization equilibrium;
- B1:** The immediate post-shock cooling zone of the bow shock;
- B2:** The post-shock cooling zone of the jet shock.

In HH 204, the relative velocity between the unshocked jet and the working surface is very low ($\approx 15 \text{ km s}^{-1}$), so the jet shock is much weaker than the bow shock, implying that the emission from zone B2 can be neglected compared with B1. Zones A1 and A2 should have similar conditions, and so can be merged into a single zone with density n_A and temperature T_A . Although the zone B1 should have a range of temperatures, for simplicity we assume a single characteristic temperature T_B . The density of zone B is found by assuming pressure equilibrium with zone A: $n_B = n_A T_A / T_B$. We define f_B for a given ion as the fraction of the total ionic emission measure, $\int n_e n_{\text{ion}} dz$, that comes from zone B, with the remainder, $f_A = 1 - f_B$, coming from zone A.

The appropriate value of T_B is rather uncertain, since it depends on the non-equilibrium evolution of ionization and temperature in the post-shock radiative relaxation layer. Most published shock models (Cox & Raymond 1985; Sutherland & Dopita 2017) are calculated on the assumption that the far upstream and downstream ionization states are determined by the radiation from the shock itself. Care must therefore be exercised when translating their results to cases such as HH 204, where external irradiation from O stars is a dominant factor. The curved bow shock in HH 204 should give a range of shock velocities, up to a maximum of $V \approx 84 \text{ km s}^{-1}$ (assuming the pre-shock medium is stationary). In principle, this corresponds to post-shock temperatures as high as $2 \times 10^5 \text{ K}$, but the gas at such temperatures will be too highly ionized to significantly emit optical lines. The cooling timescale is generally shorter than the recombination timescale, so the gas is over-ionized as it cools. It is only when the temperature falls below about $50\,000 \text{ K}$ that the abundance of O^{++} becomes significant (e.g., Fig. 11 of Allen et al. 2008), allowing the emission of the optical [O III] lines. A similar situation is seen



Reference frame
of central source

Figure 4. A simple model for the principal working surface of the HH 204 jet. The shocked gas can be divided conceptually into 4 zones: A1, A2, B1, and B2 (see text for details).

in middle-aged supernova remnants, such as the Cygnus Loop (Raymond et al. 2020).

We look for solutions where both T_A and T_B are constant along the slit, so that any spatial variation in the temperature diagnostics is driven primarily by variation in f_B . Although the density diagnostics do show a gradient with position, both $T(\text{[O III]})$ and $T(\text{[S III]})$ are relatively insensitive to density, so for simplicity we assume n_A is constant. We use the Python library PyNeb to calculate the per-zone emission coefficients, $j(T_A, n_A)$ and $j(T_B, n_B)$, for each emission line. For a given diagnostic line pair, 1 and 2, the ratio is calculated as

$$R_{12} = \frac{(1 - f_B) j_1(T_A, n_A) + f_B j_1(T_B, n_B)}{(1 - f_B) j_2(T_A, n_A) + f_B j_2(T_B, n_B)}. \quad (2)$$

This is then fed into PyNeb's `getTemDen` function to find the equivalent single-zone temperature that would give the same ratio (assuming a density of n_A). It is clear from equation (2) that for $f_B = 0$ one must recover $T_e = T_A$ and that for $f_B = 1$ one must recover $T_e = T_B$. But for intermediate values of f_B , the derived temperature will differ between ions because of variations in the temperature sensitivity of the diagnostic ratios.

We first investigate the case of a common f_B for all ions, but we find that this is unable to reproduce the observations. This is demonstrated in Figure 5a, which

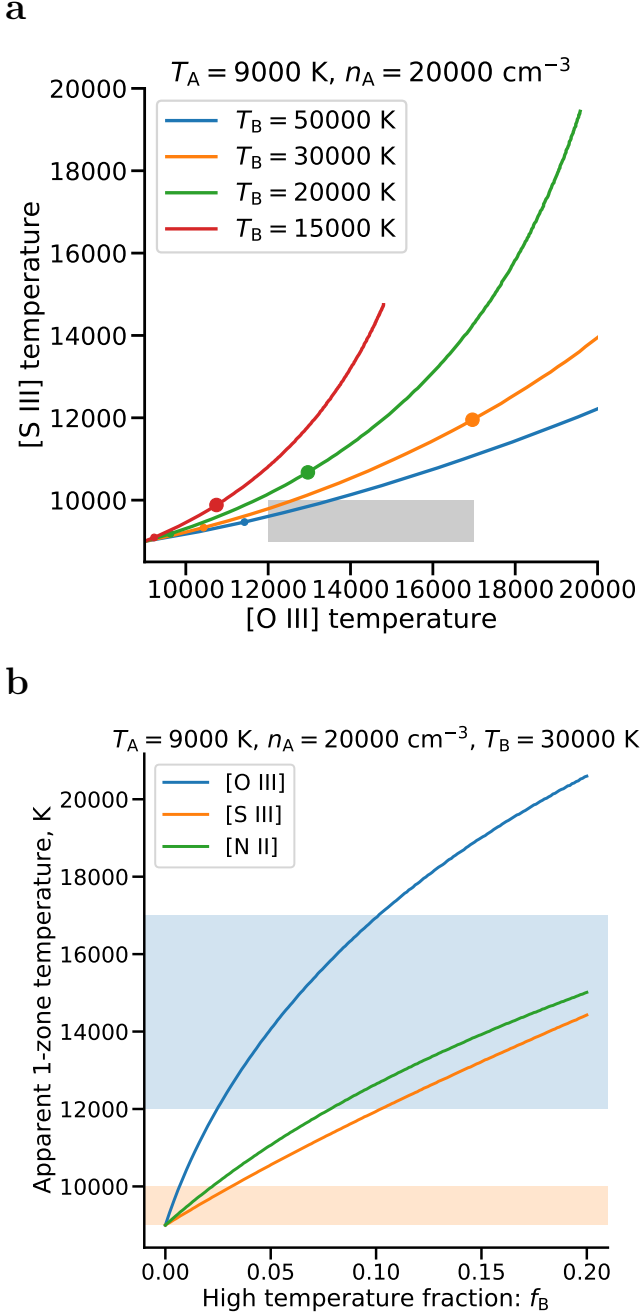


Figure 5. Simple two-zone model for spatial variations in temperature diagnostics. (a) Correlation between derived T_e from $[\text{O III}]$ and $[\text{S III}]$ lines, assuming that the fraction f_B of ionic emission measure that arises in the hot component (with temperature T_B) is the same for both ions. Values of $f_B = 0.01$ (small dots) and $f_B = 0.1$ (large dots) are indicated on each curve. The gray rectangle shows the observed range of values, which cannot be explained under this assumption (see text). (b) Derived T_e for $[\text{O III}]$, $[\text{S III}]$, and $[\text{N II}]$ lines as a function of f_B , assuming $T_B = 30000 \text{ K}$. Colored bands show the observed ranges, which imply that $f_B([\text{O III}])$ must be larger than for the other ions (see text).

shows the relation between $T_e([\text{O III}])$ and $T_e([\text{S III}])$ for 4 different values of T_B between 15 000 and 50 000 K. We set $T_A = 9000 \text{ K}$ and $n_A = 20000 \text{ cm}^{-3}$ in all cases and f_B increases from left to right along each curve. The gray rectangle shows the observed range of temperatures along the spectrograph slit (Figure 6): $T_e([\text{O III}])$ shows a systematic decline from $\approx 17000 \text{ K}$ near the bow shock to $\approx 12000 \text{ K}$ further away, while $T_e([\text{S III}])$ is roughly constant at 9000 to 10000 K, with no apparent correlation with $T_e([\text{O III}])$. The two-zone models with $T_B \geq 30000 \text{ K}$ all show $T_e([\text{O III}]) > T_e([\text{S III}])$ as f_B increases, but this is insufficient to explain the observations. For example, in order to achieve $T_e([\text{O III}]) = 17000 \text{ K}$ the models predict $T_e([\text{S III}]) > 11000 \text{ K}$, which is significantly higher than observed.

In Figure 5b, we relax the assumption of a common f_B for all ions, showing separately the predicted values of $T_e([\text{N II}])$, $T_e([\text{S III}])$, and $T_e([\text{O III}])$ as a function of f_B , assuming $T_B = 30000 \text{ K}$. The ranges of observed values are shown by colored bands, blue for $[\text{O III}]$ and orange for $[\text{N II}]$ and $[\text{S III}]$. From the figure it is apparent that a decline from $f_B([\text{O III}]) \approx 0.1$ at $x = 0$ to $f_B([\text{O III}]) \approx 0.02$ for $x > 5 \text{ mpc}$ is required to explain the $T_e([\text{O III}])$ profile, whereas $f_B([\text{S III}]) < 0.01$ and $f_B([\text{N II}]) < 0.01$ is required at all positions.

It is not surprising that f_B should vary between ions since the photoionization equilibrium ion fraction of O^{2+} from zone A is much lower than that of N^+ or S^{2+} . Assuming $f_B \ll 1$, then the ionic abundances given in the ‘‘Cut 1, HH 204’’ column of Table 4 correspond to zone A. These yield $\text{O}^{2+}/\text{O} = 0.005$ and $\text{S}^{2+}/\text{S} = 0.61$ if the abundances of unobserved ion stages are negligible. The lack of $[\text{N III}]$ lines means that N^+/N cannot be estimated directly, but is likely of order unity. The fact that O^{2+} is only present in trace amounts in the photoionization equilibrium gas means that the relative contribution from the post-shock cooling zone is much larger than for S^{2+} and N^+ . This is confirmed by emission line imaging of HH 204 (Weilbacher et al. 2015), which shows a morphology in $[\text{S III}]$ and $[\text{N II}]$ that is clearly dominated by the compact jet bullet, whereas the emission in $[\text{O III}]$ is more diffuse within the parabolic envelope of the bow shock.

REFERENCES

- Allen, M. G., Groves, B. A., Dopita, M. A., Sutherland, R. S., & Kewley, L. J. 2008, ApJS, 178, 20
- Cox, D. P., & Raymond, J. C. 1985, ApJ, 298, 651
- Doi, T., O'Dell, C. R., & Hartigan, P. 2002, AJ, 124, 445
- . 2004, AJ, 127, 3456
- García-Díaz, M. T., Henney, W. J., López, J. A., & Doi, T. 2008, RMxAA, 44, 181
- Kissler-Patig, M., Pirard, J. F., Casali, M., et al. 2008, A&A, 491, 941
- Muench, A. A., Lada, E. A., Lada, C. J., & Alves, J. 2002, ApJ, 573, 366
- O'Dell, C. R. 2009, PASP, 121, 428
- O'Dell, C. R., & Doi, T. 2003, AJ, 125, 277
- O'Dell, C. R., Ferland, G. J., Henney, W. J., et al. 2015, AJ, 150, 108
- O'Dell, C. R., Hartigan, P., Lane, W. M., et al. 1997, AJ, 114, 730
- O'Dell, C. R., & Wong, K. 1996, AJ, 111, 846
- Raymond, J. C., Chilingarian, I. V., Blair, W. P., et al. 2020, ApJ, 894, 108
- Rosado, M., de La Fuente, E., Arias, L., & Le Coarer, E. 2002, in Revista Mexicana de Astronomía y Astrofísica Conference Series, Vol. 13, Revista Mexicana de Astronomía y Astrofísica Conference Series, ed. W. J. Henney, W. Steffen, L. Binette, & A. Raga, 90–93
- Sutherland, R. S., & Dopita, M. A. 2017, ApJS, 229, 34
- Weilbacher, P. M., Monreal-Ibero, A., Kollatschny, W., et al. 2015, A&A, 582, A114